ROYAL SOCIETY OF CHEMISTRY

Developing highly reversible Li–CO₂ batteries: from on-chip exploration to practical application†

Manman Wang, [iD] ‡ᵃ Kai Yang,‡*ᵃᵇ Yuchen Ji,‡ᵇ Xiaobin Liao, [iD] ᶜ Guangpeng Zhang,ᵃ Mateus G. Masteghin, [iD] ᵃ Nianhua Peng,ᵈ Filipe Richheimer,ᵉ Huanxin Li,ᶠ Jianan Wang, [iD] ᵍ Xinhua Liu, [iD] ʰ Shichun Yang,ʰ Enrico Petrucco,ⁱ Paul Shearing, [iD] ʲ Fernando A. Castro,ᵃᵉ S. Ravi P. Silva, [iD] ᵃ Yan Zhao, [iD] ᶜ Feng Pan [iD] *ᵇ and Yunlong Zhao [iD] *ᵃᵉᵏ

Li–CO₂ batteries (LCBs) hold significant potential for meeting the energy transition requirements and mitigating global CO₂ emissions. However, the development of efficient LCBs is still in its early stages, necessitating the search for highly effective electrocatalysts and a deeper understanding of their mechanisms. To address these challenges, we have designed a versatile on-chip electrochemical testing platform, which enables simultaneous catalyst screening and *in-situ* analysis of the chemical composition and morphological evolution of reaction products. Six different metal nanoparticle catalysts were evaluated and it was found that Pt-based LCBs demonstrated a low overpotential (∼0.55 V). The reaction pathways and reversible nature of the LCBs were studied using *in situ* electrochemical Raman spectroscopy and atomic force microscopy, and were supported by *ab initio* calculations. As a result of the platform studies, LCB coin cells and pouch cells were fabricated which demonstrated high capacity, stability, and an energy efficiency of up to 90%. A multi-modal lab-on-a-chip platform has a wide range of applications in other systems, such as metal–air batteries, electrocatalysts, fuel cells, and photoelectrochemical systems, thereby opening up new opportunities for rapid catalyst screening, mechanism investigation, and the development of practical applications.

Broader context

The development of new negative emission technologies, together with advanced multimodal characterization and testing methodologies are imperative for expediting the construction of a sustainable future. As a promising next-generation negative emission technology, lithium–CO₂ batteries (LCBs) as advanced energy storage devices have garnered substantial attention due to their distinctive ability to utilise CO₂ as the reactant. Nonetheless, the development of efficient LCBs is still in its nascent stages with challenges such as large overpotential, low energy efficiency, and poor reversibility, which underscore the need not only for rapid exploration of highly effective electrocatalysts but also for an in-depth investigation for a more profound comprehension of their underlying mechanisms. The conventional method of electrocatalyst exploration for LCBs, which predominantly rely on a trial-and-error approach and unimodal characterization/testing techniques, are both inefficient and time-consuming. Consequently, the establishment of a streamlined material property testing platform that permits rapid catalyst screening and multimodal characterisation with superior temporal and nano-scale spatial resolution is imperative for achieving a more comprehensive understanding, informed decision-making, and optimal design of this emergent technology. In this work, we develop a pioneering multimodal lab-on-a-chip electrochemical testing platform to simultaneously achieve efficient catalyst screening (deterministic electrocatalyst evaluation and operation condition optimization) and integrated *in situ* probing of CO₂ conversion electrochemistry (decoupled potential analysis, product chemical composition, and morphological evolution) for high-performance LCBs. The implementation of this multimodal platform is anticipated to substantially unlock novel prospects for fast catalyst screening, mechanism investigation, and practical applications, spanning from nanoscience and technology to state-of-the-art negative emission technologies (LCBs and other electrocatalyst-based systems).

ᵃ *Advanced Technology Institute, Department of Electrical and Electronic Engineering, University of Surrey, Guildford, Surrey, GU2 7XH, UK. E-mail: kai.yang@surrey.ac.uk*

ᵇ *School of Advanced Materials, Peking University, Shenzhen Graduate School, Shenzhen 518055, China. E-mail: panfeng@pkusz.edu.cn*

ᶜ *State Key Laboratory of Advanced Technology for Materials Synthesis and Processing, Wuhan University of Technology, Wuhan 430070, China*

ᵈ *Surrey Ion Beam Centre, University of Surrey, Guildford, Surrey, GU2 7XH, UK*

ᵉ *National Physical Laboratory, Teddington, Middlesex, TW11 0LW, UK*

ᶠ *Department of Engineering, University of Cambridge, 9 JJ Thomson Avenue, Cambridge, CB3 0FA, UK*

ᵍ *Department of Environmental Science and Engineering, State Key Laboratory of Multiphase Flow in Power Engineering, Xi'an Jiaotong University, 28 Xianning West Road, Xi'an 710049, China*

ʰ *School of Transportation Science and Engineering, Beihang University, Beijing, 100191, China*

ⁱ *Johnson Matthey Technology Centre, Blounts Court, Sonning Common, Reading, UK*

ʲ *Electrochemical Innovation Lab, Department of Chemical Engineering, University College London, London, WC1E 7JE, UK*

ᵏ *Dyson School of Design Engineering, Imperial College London, London, SW7 2BX, UK. E-mail: yunlong.zhao@imperial.ac.uk*

† Electronic supplementary information (ESI) available. See DOI: https://doi.org/10.1039/d3ee00794d

‡ These authors contributed equally to this work.

3960 | *Energy Environ. Sci.*, 2023, **16**, 3960–3967

This journal is © The Royal Society of Chemistry 2023

Introduction

Metal–CO_2 batteries,[1] including Li/Na–CO_2 batteries[2,3] and Zn/Al–CO_2 batteries,[4,5] have garnered considerable attention as a potential solution to the increasing energy consumption[6,7] and persistent CO_2 emissions[8,9] due to their dual functions of energy storage/conversion and effective CO_2 utilisation.[10] Among these batteries, Li–CO_2 batteries (LCBs) stand out as the leading candidate, as they possess a high theoretical specific energy density of approximately 1876 W h kg^{-1} and a relatively high theoretical equilibrium potential of 2.8 V vs. Li/Li$^+$.[10,11] Despite the rapid progress made in the study of LCBs in recent years, LCBs remain in their early stages of development compared to lithium–ion or lithium–air batteries.[10,12]

Much effort has been dedicated to exploring efficient cathode catalysts to facilitate reversible carbon dioxide conversion through the use of carbon materials,[13–18] precious-metal-based materials (e.g., Ir-based[19–21] and Ru-based composites[22,23]), transition metal carbides/oxides/sulphides,[24–31] and metal/covalent–organic-framework-derived composites.[32–34] Nonetheless, the charge potentials obtained using these electrocatalysts typically exceed 3.5 V, which is significantly higher than the theoretical charge potential of LCBs (~ 2.8 V). Furthermore, the high polarization, resulting from the incomplete decomposition of discharge products during the charging process, can result in low energy efficiency, electrolyte decomposition, and degradation of battery performance. Hence, there is an urgent need for effective methods to rapidly screen for highly efficient catalysts to accelerate the development of LCBs.

On the other hand, the reaction mechanisms of LCBs are complex and influenced by factors such as catalyst species, electrolyte choice, sample variability, and operating conditions. The use of non-active binders, additives, and conductive agents complicates the characterization and quantification of the formation and decomposition of reaction products during the discharge and charge processes. Therefore, a robust and versatile testing platform, coupled with sophisticated characterisation techniques and the option to use carbon-free cathodes, is crucial for gaining a deeper understanding of the electrochemical mechanisms precisely.

In this study, we systematically evaluate a series of candidate catalysts for their potential to promote the conversion reaction and investigate their reversibility and reaction pathways. To this end, we developed a versatile and reliable lab-on-a-chip platform that integrates advanced testing and characterisation techniques, including a three-electrode configuration, in situ electrochemical Raman (EC-Raman) spectroscopy, in situ Fourier transform infrared (EC-FTIR) spectroscopy and electrochemical atomic force microscopy (EC-AFM) (Fig. 1a and 2a). To minimize experimental variability, key parameters such as the dimension and location of electrodes, the type and amount of electrolyte, and test conditions are rationally designed and precisely controlled. The candidate catalysts, which include high-density nanoparticles of Pt, Au, Ag, Cu, Fe, and Ni were prepared via E-beam deposition. Pt-based on-chip batteries yield remarkable lowest polarization (0.55 V), highest

reversibility and new reaction pathways, which agree with DFT calculations. Finally, as a proof-of-principle of macroscopic applicability, the optimised catalysts and testing parameters from the lab-on-a-chip platform were applied in LCB coin cells and pouch cells to demonstrate the practical potential of LCBs.

The Pt-based coin cells and pouch cells are assembled, showing excellent battery performance (a maximum capacity of 41 466 mA h g^{-1}, an ultra-high energy efficiency of $\sim 80\%$ and over 100 stable cycles at 200 mA g^{-1}) and indicating great commercial potential.

Results and discussion

Platform design, fabrication, and characterisation

Our strategy for creating the lab-on-a-chip platform involves four key steps (see Supplementary Methods for details (ESI†) and Fig. 1b). First, geometry-controlled Au and Cu electrodes were deposited on a SiO_2/Si wafer via E-beam evaporation, serving as cathode and anode current collectors, respectively (Fig. S1, ESI†). Two current collectors were designed for each electrode to avoid poor electrical contact arising from misalignment, and to provide the possibility of concurrent testing for electrode material degradation studies in the future.[35] Second, nanoparticle catalysts (Pt, Au, Ag, Cu, Fe, and Ni) with a thickness of 100 nm were deposited on a wafer via E-beam evaporation (Fig. 1c) using shallow masks of the same size (Fig. S1b, ESI†). Third, Li metal anodes were deposited via thermal evaporation in an Ar glovebox with a shallow mask (Fig. S1c, ESI†). Finally, the on-chip devices were cut off from the wafer, equipped with inlet and outlet needles and an Ag/AgCl reference electrode, and encapsulated by a glass slide and epoxy resin for electrolyte injection and testing. To fit with different testing conditions, on-chip LCBs with slightly different sizes and geometries were fabricated.

Optical microscopy was first used to characterise all the key steps in the fabrication flow (Fig. 1b and Fig. S2, ESI†). For smaller size devices, 4 arrays with twelve cathodes can be made on a 4-inch wafer (Fig. 1b), while 2 arrays can be made for larger devices (Fig. S2, ESI†). To characterise the morphology and crystallographic structure of the as-deposited Pt, Au, Ag, Cu, Fe, and Ni cathode catalysts, scanning electron microscopy (SEM) and grazing incidence X-ray diffraction (GIXRD) analyses were conducted (Fig. S3 and S4, ESI†). All these catalysts show a cubic ($Fm\bar{3}m$) structure and a uniform high-density nanoparticle morphology. The nano-scale morphology of the Pt-based electrode was also analysed in detail using AFM as shown in Fig. 1d, which was consistent with SEM observation.

Catalyst screening and in situ multimodal probing

With these characterisation results, we first considered whether the on-chip devices were functional and electrochemically stable after the injection of a CO_2-saturated electrolyte. A three-electrode electrochemical testing configuration was used in which the full-cell voltage and decoupled individual electrode potentials could be measured during galvanostatic
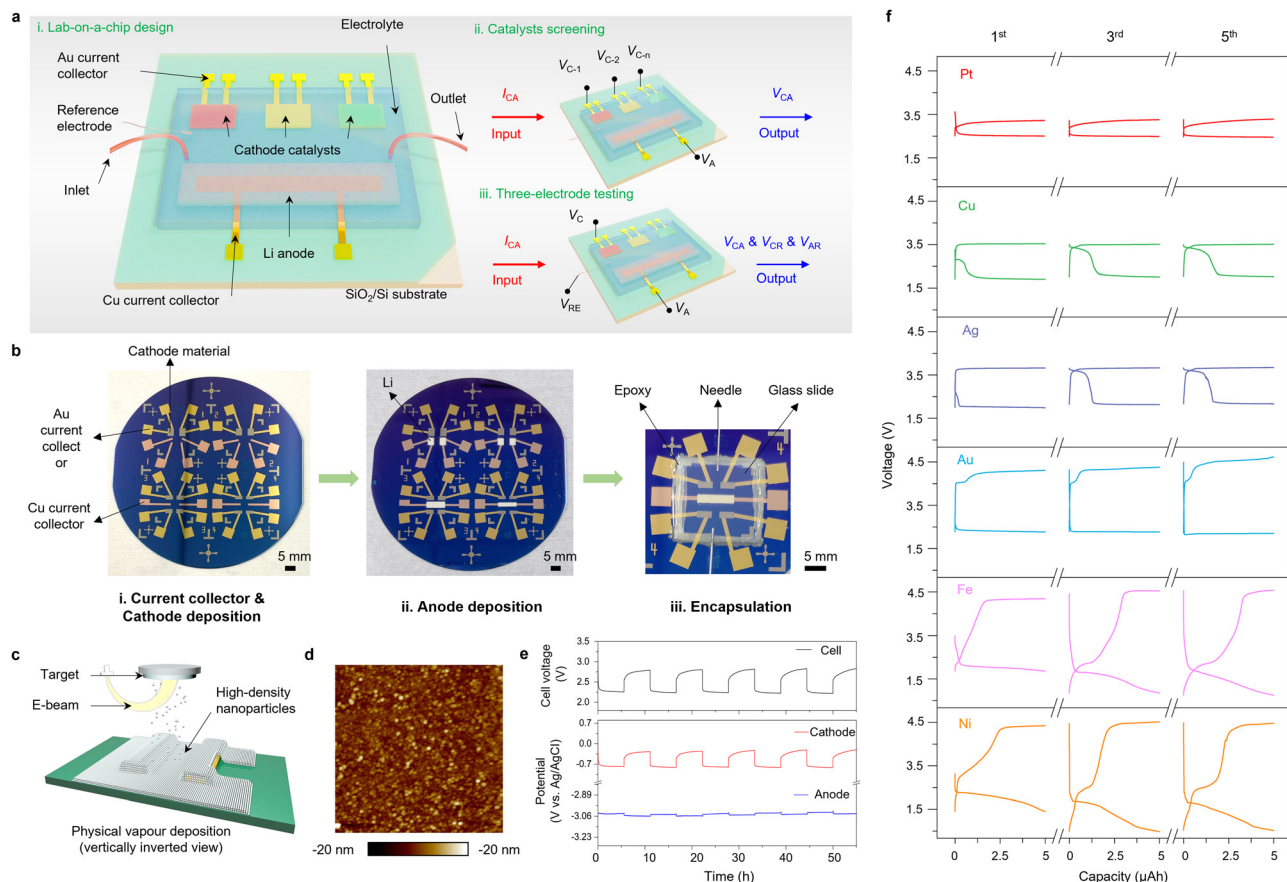
This journal is © The Royal Society of Chemistry 2023

Energy Environ. Sci., 2023, **16**, 3960–3967 | **3961**

Fig. 1 Design of a lab-on-a-chip platform for catalyst screening and electrochemical testing. (a) Schematic illustration of the (i) designed on-chip LCB array, which is capable of (ii) screening cathode catalysts and (iii) performing three-electrode testing. (b) Optical image of on-chip Li–CO₂ devices at different fabrication steps. (c) Loading a high-density nanoparticle electrocatalyst using thermal evaporation. (d) Nano-scale morphology of a Pt-based electrode. (e) Three-electrode galvanostatic discharge–charge test of a Pt-based on-chip LCB at a constant current of 1 μA: profiles of full-cell voltage, cathode potential, and anode potential (*versus* Ag/AgCl reference electrode). (f) Catalyst screening: the 1st, 3rd, and 5th discharge–charge profiles of six different metal catalysts (Pt, Cu, Ag, Au, Fe, and Ni)-based on-chip LCBs, with a limiting capacity of 5 μA h and at a constant current of 1 μA.

cycling. Fig. 1e shows the curves of full-cell voltage and decoupled individual potentials of the Pt cathode and the Li anode over five cycles at a constant current of 1 μA. The full-cell voltage follows a similar trend to the cathode potential, and only a minimal potential change of approximately 0.01 V was observed at the anode side during the 55 hours of on-chip LCB cycling without additional perfusion of CO₂ or change of the electrolyte. This indicates that the Li electrode and the electrolyte on this on-chip device remain electrochemically stable during testing.

After confirming its testing functionality and electrochemical stability, we considered whether this on-chip platform could be used for catalyst screening. Standard galvanostatic discharge–charge tests were performed at a current density of 1 μA with a constant capacity of 5 μA h. Here, we compare the 1st, 3rd, and 5th discharge–charge profiles of different catalyst devices (Fig. 1f, see all profiles in Fig. S5, ESI†). Among these catalysts, the Pt-based device displays a low charge potential of 2.85 V and the smallest overpotential of 0.55 V. The subsequent cycles also sustain a consistent shape and potential. In contrast, the Cu- and Ag-based devices exhibit similar profiles, with

a relatively low charge potential of around 3.1 V and two discharge plateaus, but yield limited reversibility and low energy efficiency. Although the Au-based device shows good cycling stability, the charge potential is up to 4.2 V, resulting in an excessive overpotential and low energy efficiency. Fe- and Ni-based devices do not exhibit significantly improved electrochemical performance in the presence of catalysts.

Notably, the charge potential of 2.85 V obtained from the Pt-based on-chip LCB is the lowest charge potential for an LCB in the reported literature of electrocatalysts (excluding the photo-electrocatalysis works), and the closest to the theoretical charge potential (Table S1, ESI†). To understand this extraordinary result and the corresponding reaction process, we investigated the evolution of the chemical composition and morphology of the reaction products during discharge–charge *via* the on-chip *in situ* EC-Raman spectroscopy, *in situ* FTIR spectroscopy and EC-AFM (Fig. 2a). First, *in situ* EC-Raman spectroscopy of the Pt-based on-chip LCB was performed with the potential ranging from an open-circuit potential (OCP) of ∼2.9 V to 2.2 V and back to 2.9 V at a current density of 2 μA (Fig. 2b–d). During the discharging process, two peaks centred at ∼1085 cm⁻¹ and

3962 | *Energy Environ. Sci.*, 2023, **16**, 3960–3967

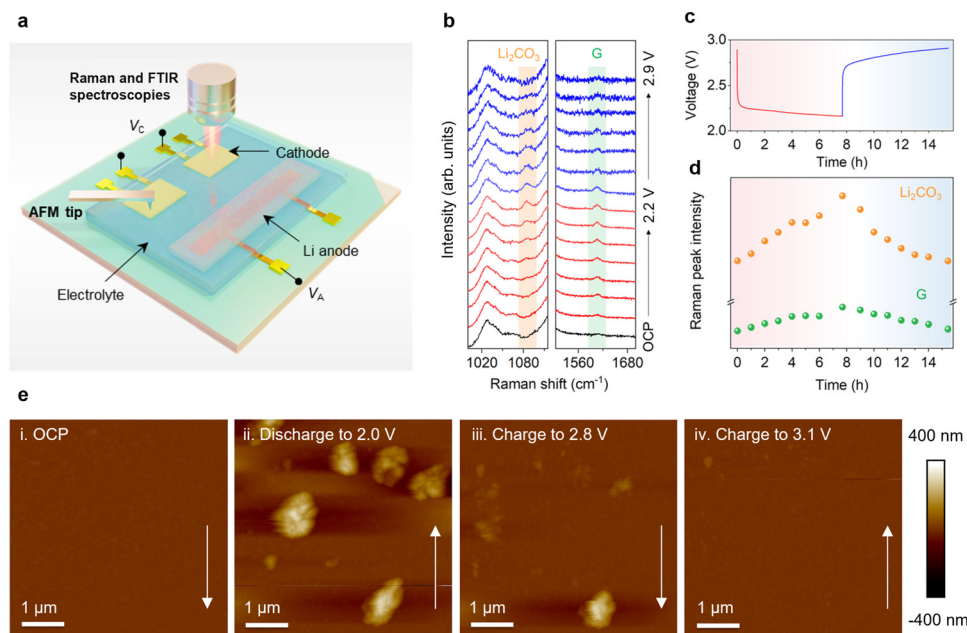This journal is © The Royal Society of Chemistry 2023

Fig. 2 The lab-on-a-chip platform for *in situ* probing of the chemical composition and morphological evolution. (a) Schematic illustration of the designed on-chip LCB array with *in situ* EC-Raman spectroscopy and EC-AFM functionality. (b) EC-Raman spectra of the Pt cathode recorded during the corresponding galvanostatic discharge–charge process. Black, red, and blue curves represent the battery in the open-circuit potential (OCP) state, the discharge state, and the charge state, respectively. (c) Galvanostatic discharge–charge test of the Pt-based on-chip LCB at a constant current of 2 μA. (d) Raman peak intensity changes of Li_2CO_3 (~1085 cm^{-1}) and carbon (G band, ~1604 cm^{-1}) during the corresponding discharge–charge process. (e) *In situ* EC-AFM topographical images of the Pt cathode in a CO_2 atmosphere obtained at (i) OCP, (ii) discharge to 2.0 V, (iii) charge to 2.8 V, and (iv) charge to 3.1 V. The black arrows represent the scanning direction.

~1604 cm^{-1} appeared and increased gradually, which correspond to Li_2CO_3[36,37] and the G band of carbon,[38–40] respectively (Fig. 2b and d). During the charging process, the normalized intensities of Raman scattering from the Li_2CO_3 and carbon species decrease simultaneously, and after the charging was completed, the peak intensities return to the same level as that in the OCP state. During these processes, no significant changes in other peaks were observed (Fig. S6, ESI†). Considering that the cathode surface is uniform and free of interference from other carbonaceous components and additives (such as Li_2CO_3), these data accurately reflect the evolution of the chemical composition in Pt-based on-chip LCBs. Moreover, *in situ* FTIR measurement can also be conducted on the Pt-based on-chip LCBs (Fig. S7, ESI†). During the discharging process, the Li_2CO_3 peaks gradually emerged with the generation of the discharging product. During the charging process, the intensity of Li_2CO_3 peaks gradually reduced and completely disappeared when charged to 5 μA h. The *in situ* FTIR spectral observation of the Cu- and Ni-based on-chip LCBs (Fig. S8 and S9, ESI†) indicated that chemical side reactions might occur to generate by-products and decrease the reversibility.

In addition, the *in situ* EC-AFM test was performed to study the morphological evolution of the Pt-based on-chip LCB (the *in situ* AFM setup is shown in Fig. S10, ESI†). First, we conducted the EC-AFM test in a pure Ar atmosphere as a control. As shown in Fig S11 (ESI†), the topography of the cathode surface remains unchanged throughout the whole discharge and charge process without additional products

nucleating, growing, or disappearing. Then, CO_2 was introduced into our on-chip system followed by EC-AFM measurements (Fig. 2e). The surface was clean in the OCP state, but during the discharging process, particles gradually formed, and when it discharges to 2.0 V, the diameter of the particles had grown to around 400 nm. During the subsequent charging process, the particles gradually become smaller. After charging, all the particles disappeared, and the cleanliness/smoothness was similar to that in the initial OCP state. Combined with the *in situ* EC-Raman spectroscopy and *in situ* FTIR spectroscopy results, these results indicate that for Pt-based on-chip LCBs, only Li_2CO_3 and carbon species are formed during the discharging process.

In the subsequent charging process, even at an extremely low charging potential, complete decomposition of both Li_2CO_3 and carbon species can still be achieved simultaneously, thus showing excellent reversibility and high energy efficiency.

Catalytic mechanism and reaction pathway investigation

After determining the reaction products and reversibility, we further investigated the catalytic mechanism and reaction pathways. We first studied the lattice plane of the Pt catalyst *via* transmission electron microscopy (TEM).

The TEM analysis image shows a homogeneous distribution of Pt nanoparticles covering the sample surface (Fig. 3a), and the selected area electron diffraction (SAED, enlarged figure in Fig. 3a) image agrees well with the GIXRD results (Fig. S4a, ESI†) and supports the proposed absence of carbides. The high-
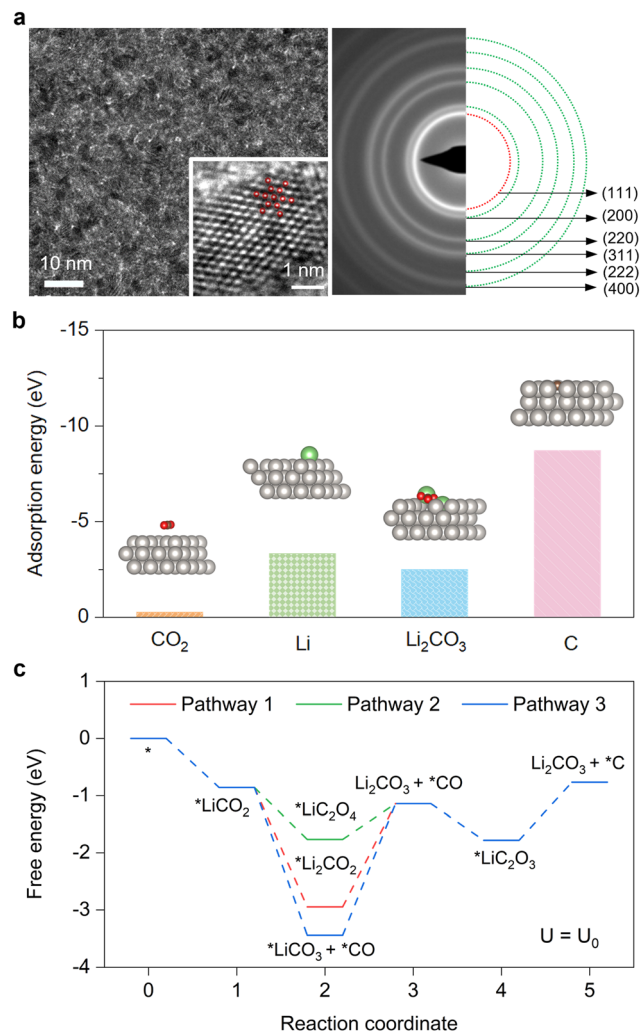
Fig. 3 Investigation of the catalytic mechanism and the reaction pathway. (a) Transmission electron microscopy (TEM) image and select area electron diffraction (SAED) image of E-beam evaporated Pt. Inset: High-resolution transmission electron microscopy (HRTEM) image overlayed by the atomic arrangement of the (111) facet showing the expected projection through the [111] zone axis. (b) Absorption energy of CO_2, Li, Li_2CO_3 and C on the Pt(111) surface. Insets show the side view of CO_2, Li and Li_2CO_3 adsorption configurations on the Pt(111) surface. Grey, Pt; green, Li; red, O; and brown, C. (c) Gibbs free energy diagram of the three reaction pathways on the Pt(111) surface during the discharging process at $U = U_0 = 2.85$ V. * Represents the Pt(111) surface.

resolution transmission electron microscopy (HRTEM) image of a representative nanoparticle can be overlayed by a series of atomic projections on the (111) plane, demonstrating the dominance of the (111) facet (Fig. 3a).

Based on the above analysis, density functional theory (DFT) calculations were performed based on the basal plane of Pt(111). We first constructed the adsorption configurations of CO_2, Li, Li_2CO_3 and C on the Pt(111) surface and calculated the corresponding adsorption energies (Fig. 3b). The adsorption energy of Li (-3.31 eV) is higher than that of CO_2 (-0.23 eV), indicating that Li has stronger adsorption than CO_2 on the Pt(111) surface, which excludes reaction pathways that begin

with the adsorption of CO_2 (* + CO_2 → *CO_2, * represents the basal plane of Pt(111)). Meanwhile, considering that the adsorption energy of the discharge product Li_2CO_3 (-2.48 eV) is lower than that of C (-8.7 eV) on the Pt(111) surface, here we hypothesised three possible reaction pathways according to recent literature[21,41–43] for the formation of Li_2CO_3 and *C (Fig. S12 and S13, ESI†). Second, the catalytic activity of Pt(111) was quantitatively investigated by the Gibbs free energy changes (ΔG) at each reaction step in these feasible pathways (Fig. 3c and Fig. S14, Table S2, ESI†). As shown in Fig. 3c, during the discharging process, the rate-determining step (RDS) in pathway 1 ($\Delta G_3 = 1.80$ eV) and pathway 3 ($\Delta G_3 = 2.30$ eV) is step 3, while the RDS in pathway 2 ($\Delta G_5 = 1.01$ eV) is step 5. As pathway 2 possesses the smallest ΔG in the RDS, it represents the most feasible pathway for the formation of Li_2CO_3 and C on the Pt(111).

Electrochemical evaluation of macroscale LCBs

Finally, we consider whether the lab-on-chip platform for catalyst screening provides reliable guidance for practical technology development, by applying the selected Pt catalyst at the coin cell and pouch cell level. The Pt catalysts were E-beam deposited on carbon paper (Pt@CP), serving as the cathode for LCB coin cells and pouch cells (Fig. S15, ESI†). We first evaluated the electrochemical performance of coin cells by comparing the deep discharge in a CO_2 and an Ar atmosphere-controlled chamber (Fig. S16, ESI†). In the CO_2 atmosphere, the Pt-based LCB coin cells yield a high capacity of 41 470 mA h g^{-1} at a current density of 100 mA g^{-1} (the specific areal capacity is around 4.15 mA h cm^{-2} based on the areal mass loading of the catalyst in the electrode), while only 340 mA h g^{-1} was obtained in the Ar atmosphere (Fig. 4a). In comparison, the carbon paper alone delivered a negligible capacity in the CO_2 atmosphere (Fig. S17, ESI†). This indicates that the high discharge capacity of the LCBs arises from the reactions involving Pt and CO_2, rather than other parasitic reactions, such as electrolyte decomposition. The discharge–charge performance was then evaluated at current densities of 100, 200 and 500 mA g^{-1} with a limiting capacity of 1000 mA h g^{-1} (Fig. 4b). Notably, the LCB coin cells delivered a low over-potential of 0.35 V at a current density of 100 mA g^{-1} and maintained low levels of 0.75 V and 0.96 V at 200 mA g^{-1} and 500 mA g^{-1}, respectively, which lead to the high energy efficiency of up to 90% —much higher than those reported in current electrocatalysis literature (Table S1, ESI†). It should be mentioned that the diameter of the carbon fibre in carbon paper is around 10 μm, leading to a large volume proportion of the non-catalytic composition toward CO_2 conversion. And the dense surface of the deposited thin-film platinum catalyst may also limit the reaction kinetics. Thus, the discharge voltage plateau decreases with increasing current density. Even so, the Pt catalyst has been confirmed to deliver an excellent CO_2 conversion for Li–CO_2 batteries especially for the outstanding low overpotential and high energy efficiency performance. To cut down the utilization cost of Pt while optimizing its catalytic performance, the following strategies can be considered: (1)
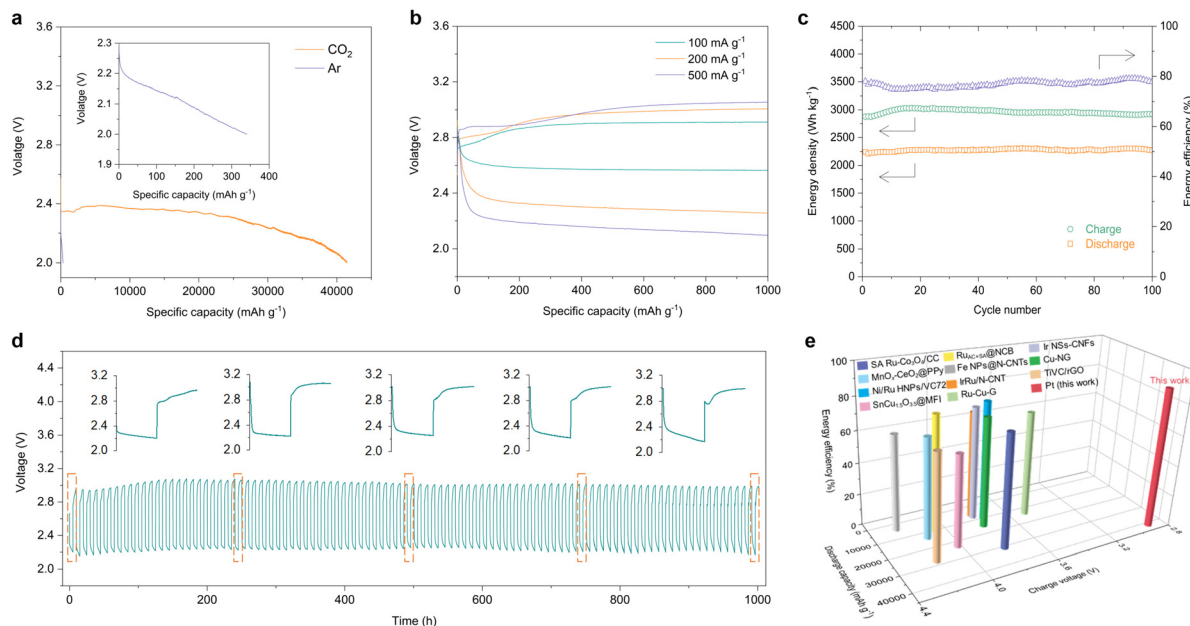
3964 | *Energy Environ. Sci.,* 2023, **16**, 3960–3967

This journal is © The Royal Society of Chemistry 2023

Fig. 4 Electrochemical performance of Pt-based LCB coin cells. (a) Full discharge curves of Pt-based LCB coin cells in the CO_2 and Ar atmosphere (inset) at a current density of 100 mA g^{-1}. (b) Discharge–charge curves of Pt-based coin cells at different current densities of 100 mA g^{-1}, 200 mA g^{-1} and 500 mA g^{-1} with a limiting capacity of 1000 mA h g^{-1}. (c) Energy density and energy efficiency *versus* cycle number profiles. (d) Cycling performance with typical discharge–charge curves of Pt-based LCB coin cells at a current density of 200 mA g^{-1} with a limiting capacity of 1000 mA h g^{-1}. (e) Comparison of the Pt-based LCB coin cell performance with those of other reported studies.

porous carbon fibres (*e.g.*, electrospinning carbon nanofibers, self-supported carbon nanotubes or graphene membranes) with high conductivity, hierarchical pore size distribution and mechanical strength should be used as substrates; (2) creating three-dimensional porous nanostructures or increasing the specific surface to expose effective catalytic sites thus contributing to enhanced battery performance; (3) crystal engineering (*e.g.*, defects, heterojunctions, non-equilibrium heat treatment, *etc.*) to intensify preferred orientations for CO_2 conversion; (4) introducing cheap transition metals (TMs) and synthesizing Pt/TM alloy catalysts with the synergistic balance between the performance and the cost. The coin cells were operated at a current density of 200 mA g^{-1} for 1000 hours (100 cycles), showing outstanding cycling stability with a sustained high energy density and energy efficiency ($\sim$80%) (Fig. 4c and d). To further probe the mechanism associated with the Pt

catalysts in Li–CO_2 coin cells, *ex situ* SEM and Raman scattering characterization studies were conducted. Fig. S18 (ESI†) displays the morphology of the pristine state, the discharge state and the recharge state of Pt@CP. It can be observed that some thin film-like discharge products were generated and accumulated on the surface of carbon paper fibres. After recharging, almost all the discharge products disappeared on the surface of the carbon fibres, indicating the good reversibility of Pt. The Raman spectra further confirmed the reversible formation and decomposition of Li_2CO_3 in the discharge and charge process (Fig. S19, ESI†). It is worth noting that the ratio of the carbon D and G peak intensities (I_D/I_G) for the discharge products is significantly higher than those for the pristine state and the charging state, which further suggests that amorphous carbon was generated during the discharge process and decomposed during the recharging process. Here, we compare our results
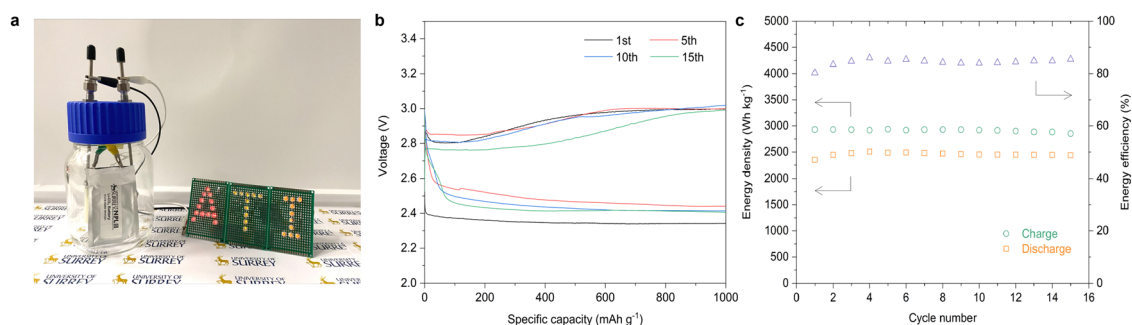

Fig. 5 LCB pouch cell performance. (a) Photograph of the Pt-based LCB pouch cell lighting up the LED array. Discharge–charge curves (b) and energy density and energy efficiency *versus* cycle number profiles (c) of the Pt-based LCB pouch cell with a limiting capacity of 1000 mA h g^{-1}.

with other reported typical results in terms of the full discharge capacity, charge potential and energy efficiency, indicating the huge advantage of our LCB performance in these areas. (Fig. 4e). As a demonstration of the potential for further macroscopic applications, we assembled single-layer LCB pouch cells (Fig. S20, ESI†). When exposed to the CO_2 atmosphere, the pouch cells provided an open-circuit voltage of 2.7 V (Fig. S20, ESI†) and were able to continuously power a light-emitting diode array board (Fig. 5a). The discharge–charge profiles show that the pouch cells were stably operated with a limiting capacity of 1000 mA h g^{-1} (Fig. 5b). The overpotential is about 0.6 V and the charge potential is $\sim$3 V. During the 15 cycles, the LCB pouch cells yield a discharge energy density of $\sim$2450 W h kg^{-1} with an energy efficiency of 85% (Fig. 5c). Such a high energy density and extremely high energy efficiency make the LCBs highly competitive for practical applications, particularly in stationary energy storage.

Conclusions

In summary, we have rationally designed and developed a lab-on-a-chip LCB platform that features functionality for three-electrode electrochemical testing, catalyst screening and *in situ* probing of chemical composition and morphological evolution. Through this platform, we identified the E-beam-deposited Pt nanoparticles as some of the most efficient catalysts from a series of typical candidates that can promote LCB reactions and quantified their reversibility. As a proof of principle for translation to practical applications, LCB coin cells and pouch cells were fabricated with Pt catalysts and optimal parameters, exhibiting superior performance of low overpotential, high energy efficiency and outstanding stability. These results highlight the competitive advantages of LCBs, although some technical challenges remain in practical applications, such as electrolyte evaporation and lithium-anode degradation during prolonged operation.[1,2,10,11] To address the above challenges, we hypothesise that our lab-on-a-chip LCB platform could play an important role in further explorations, including (1) screening of electrolytes with stable solvents for the LCB reaction by integrating a microfluidic system or patterning different quasi-solid electrolytes on the platform and (2) exploring different lithium-anode protection strategies or screening other pre-lithiated anodes for LCBs. More generally, this versatile and reliable platform can be well integrated with other catalyst loading techniques (summarized in Table S3, ESI†), exhibiting compatibility with the catalyst size ranging from single atoms, nanoparticles, to micrometre sizes. For the demonstration, we used the spraying coating technique (a detailed process can be found in Fig. S21, ESI†) to prepare porous activated carbon (AC) based on-chip LCBs. The on-chip devices play the same role of test and analysis (Fig. S22 and S23, ESI†) with a high loading of catalysts and are recyclable (Fig. S24, ESI†). While the commercial *in situ* cells might only suit specific situations, the demonstrated multimodal on-chip platform with the versatile catalysts and substrate material loading/testing/characterization ability, can be adapted and applied as a universal electrochemical testing and characterization platform not only for the demonstrated LCBs, but also for broader applications in other catalyst-based energy storage/conversion systems, such as metal–air batteries, fuel cells, photoelectrochemical cells or even laboratory robotics, opening opportunities for rapid and scalable screening, accurate testing, and mechanism investigations.

Author contributions

M. Wang, K. Yang and Y. Ji contributed equally to this work; K. Yang, F. Pan and Y. Zhao conceived the presented idea; Y. Zhao, K. Yang and M. Wang conceived and designed the experiments; M. Wang, K. Yang and Y. Ji performed the main experiments and analysed the data; and M. Wang, K. Yang and Y. Zhao co-wrote the paper. All authors discussed the results and revised the manuscript.

Conflicts of interest

There are no conflicts to declare.

Acknowledgements

References

1 H. Gao and B. M. Gallant, *Nat. Rev. Chem.*, 2020, **4**, 566–583.
2 Y. Qiao, J. Yi, S. Wu, Y. Liu, S. Yang, P. He and H. Zhou, *Joule*, 2017, **1**, 359–370.
3 X. Mu, H. Pan, P. He and H. Zhou, *Adv. Mater.*, 2020, **32**, 1903790.
4 F. Wang, Y. Li, X. Xia, W. Cai, Q. Chen and M. Chen, *Adv. Energy Mater.*, 2021, **11**, 2100667.
5 J. Xie, Z. Zhou and Y. Wang, *Adv. Funct. Mater.*, 2020, **30**, 1908285.
6 D. Larcher and J. M. Tarascon, *Nat. Chem.*, 2015, **7**, 19–29.
7 M. K. Debe, *Nature*, 2012, **486**, 43–51.
8 A. M. Appel, J. E. Bercaw, A. B. Bocarsly, H. Dobbek, D. L. DuBois, M. Dupuis, J. G. Ferry, E. Fujita, R. Hille, P. J. A. Kenis, C. A. Kerfeld, R. H. Morris, C. H. F. Peden, A. R. Portis, S. W. Ragsdale, T. B. Rauchfuss, J. N. H. Reek,

L. C. Seefeldt, R. K. Thauer and G. L. Waldrop, *Chem. Rev.*, 2013, **113**, 6621–6658.

9 T. Ahmad, S. Liu, M. Sajid, K. Li, M. Ali, L. Liu and W. Chen, *Nano Res. Energy*, 2022, **1**, e9120021.

10 B. Liu, Y. Sun, L. Liu, J. Chen, B. Yang, S. Xu and X. Yan, *Energy Environ. Sci.*, 2019, **12**, 887–922.

11 Z. Zhang, W.-L. Bai, K.-X. Wang and J.-S. Chen, *Energy Environ. Sci.*, 2020, **13**, 4717–4737.

12 S. Zhang, L. Sun, Q. Fan, F. Zhang, Z. Wang, J. Zou, S. Zhao, J. Mao and Z. Guo, *Nano Res. Energy*, 2022, **1**, 9120001.

13 L. Qie, Y. Lin, J. W. Connell, J. Xu and L. Dai, *Angew. Chem., Int. Ed.*, 2017, **56**, 6970–6974.

14 Y. Jin, C. Hu, Q. Dai, Y. Xiao, Y. Lin, J. W. Connell, F. Chen and L. Dai, *Adv. Funct. Mater.*, 2018, **28**, 1804630.

15 Y. Xiao, F. Du, C. Hu, Y. Ding, Z. L. Wang, A. Roy and L. Dai, *ACS Energy Lett.*, 2020, **5**, 916–921.

16 C. Hu, L. Gong, Y. Xiao, Y. Yuan, N. M. Bedford, Z. Xia, L. Ma, T. Wu, Y. Lin, J. W. Connell, R. Shahbazian-Yassar, J. Lu, K. Amine and L. Dai, *Adv. Mater.*, 2020, **32**, 1907436.

17 F. Ye, L. Gong, Y. Long, S. N. Talapaneni, L. Zhang, Y. Xiao, D. Liu, C. Hu and L. Dai, *Adv. Energy Mater.*, 2021, **11**, 2101390.

18 X. Li, J. Zhou, J. Zhang, M. Li, X. Bi, T. Liu, T. He, J. Cheng, F. Zhang, Y. Li, X. Mu, J. Lu and B. Wang, *Adv. Mater.*, 2019, **31**, 1903852.

19 J. Li, L. Wang, Y. Zhao, S. Li, X. Fu, B. Wang and H. Peng, *Adv. Funct. Mater.*, 2020, **30**, 2001619.

20 Y. Xing, Y. Yang, D. Li, M. Luo, N. Chen, Y. Ye, J. Qian, L. Li, D. Yang, F. Wu, R. Chen and S. Guo, *Adv. Mater.*, 2018, **30**, 1803124.

21 Y.-J. Rho, B. Kim, K. Shin, G. Henkelman and W.-H. Ryu, *J. Mater. Chem. A*, 2022, **10**, 19710–19721.

22 S. Yang, Y. Qiao, P. He, Y. Liu, Z. Cheng, J.-J. Zhu and H. Zhou, *Energy Environ. Sci.*, 2017, **10**, 972–978.

23 Z. Zhang, C. Yang, S. Wu, A. Wang, L. Zhao, D. Zhai, B. Ren, K. Cao and Z. Zhou, *Adv. Energy Mater.*, 2019, **9**, 1802805.

24 X. Zhang, T. Wang, Y. Yang, X. Zhang, Z. Lu, J. Wang, C. Sun, Y. Diao, X. Wang and J. Yao, *ACS Energy Lett.*, 2021, **6**, 3503–3510.

25 Y. Hou, J. Wang, L. Liu, Y. Liu, S. Chou, D. Shi, H. Liu, Y. Wu, W. Zhang and J. Chen, *Adv. Funct. Mater.*, 2017, **27**, 1700564.

26 J. Zhou, X. Li, C. Yang, Y. Li, K. Guo, J. Cheng, D. Yuan, C. Song, J. Lu and B. Wang, *Adv. Mater.*, 2019, **31**, 1804439.

27 C. Yang, K. Guo, D. Yuan, J. Cheng and B. Wang, *J. Am. Chem. Soc.*, 2020, **142**, 6983–6990.

28 S. Li, Y. Liu, J. Zhou, S. Hong, Y. Dong, J. Wang, X. Gao, P. Qi, Y. Han and B. Wang, *Energy Environ. Sci.*, 2019, **12**, 1046–1054.

29 H. Wang, K. Xie, Y. You, Q. Hou, K. Zhang, N. Li, W. Yu, K. P. Loh, C. Shen and B. Wei, *Adv. Energy Mater.*, 2019, **9**, 1901806.

30 H.-S. Kim, J.-Y. Lee, J.-K. Yoo and W.-H. Ryu, *ACS Mater. Lett.*, 2021, **3**, 815–825.

31 B. Lu, B. Chen, D. Wang, C. Li, R. Gao, Y. Liu, R. Mao, J. Yang and G. Zhou, *Proc. Natl. Acad. Sci. U. S. A.*, 2023, **120**, e2216933120.

32 S. Li, Y. Dong, J. Zhou, Y. Liu, J. Wang, X. Gao, Y. Han, P. Qi and B. Wang, *Energy Environ. Sci.*, 2018, **11**, 1318–1325.

33 X. Li, H. Wang, Z. Chen, H.-S. Xu, W. Yu, C. Liu, X. Wang, K. Zhang, K. Xie and K. P. Loh, *Adv. Mater.*, 2019, **31**, 1905879.

34 C. Jiang, Y. Zhang, M. Zhang, N.-N. Ma, G.-K. Gao, J.-H. Wang, M.-M. Zhang, Y. Chen, S.-L. Li and Y.-Q. Lan, *Cell Rep. Phys. Sci.*, 2021, **2**, 100392.

35 L. Mai, M. Yan and Y. Zhao, *Nature*, 2017, **546**, 469–470.

36 B.-W. Zhang, Y. Jiao, D.-L. Chao, C. Ye, Y.-X. Wang, K. Davey, H.-K. Liu, S.-X. Dou and S.-Z. Qiao, *Adv. Funct. Mater.*, 2019, **29**, 1904206.

37 Z. Zhao, L. Pang, Y. Su, T. Liu, G. Wang, C. Liu, J. Wang and Z. Peng, *ACS Energy Lett.*, 2022, **7**, 624–631.

38 B. Gao, X. Duan, J. Zhang, G. Wu, J. Dong and Z. Liu, *J. Phys. Chem. C*, 2008, **112**, 10789–10793.

39 M. W. Smith, I. Dallmeyer, T. J. Johnson, C. S. Brauer, J.-S. McEwen, J. F. Espinal and M. Garcia-Perez, *Carbon*, 2016, **100**, 678–692.

40 J. Wang, H. Xian, T. Peng, H. Sun and F. Zheng, *RSC Adv.*, 2015, **5**, 13607–13612.

41 B. Chen, D. Wang, J. Tan, Y. Liu, M. Jiao, B. Liu, N. Zhao, X. Zou, G. Zhou and H.-M. Cheng, *J. Am. Chem. Soc.*, 2022, **144**, 3106–3116.

42 Y. Liu, S. Zhao, D. Wang, B. Chen, Z. Zhang, J. Sheng, X. Zhong, X. Zou, S. P. Jiang, G. Zhou and H.-M. Cheng, *ACS Nano*, 2022, **16**, 1523–1532.

43 Y. Zhang, R.-L. Zhong, M. Lu, J.-H. Wang, C. Jiang, G.-K. Gao, L.-Z. Dong, Y. Chen, S.-L. Li and Y.-Q. Lan, *ACS Cent. Sci.*, 2021, **7**, 175–182.

This journal is © The Royal Society of Chemistry 2023

Energy Environ. Sci., 2023, **16**, 3960–3967 | **3967**